A Direct Grain-Boundary-Activity Correlation for CO Electroreduction on Cu Nanoparticles

Xiaofeng Feng,[†] Kaili Jiang,[‡] Shoushan Fan,[‡] and Matthew W. Kanan*,[†]

[†]Department of Chemistry, Stanford University, Stanford, California 94305, United States
[‡]Department of Physics and Tsinghua-Foxconn Nanotechnology Research Center, Tsinghua University, Beijing 100084, China

S Supporting Information

ABSTRACT: Copper catalyzes the electrochemical reduction of CO to valuable C_{2+} products including ethanol, acetate, propanol, and ethylene. These reactions could be very useful for converting renewable energy into fuels and chemicals, but conventional Cu electrodes are energetically inefficient and have poor selectivity for CO vs H_2O reduction. Efforts to design improved catalysts have been impeded by the lack of experimentally validated, quantitative structure–activity relationships. Here we show that CO reduction activity is directly correlated to the density of grain boundaries (GBs) in Cu nanoparticles (NPs). We prepared electrodes of Cu NPs on carbon nanotubes (Cu/CNT) with different average GB densities quantified by transmission electron microscopy. At

potentials ranging from −0.3 V to −0.5 V vs the reversible hydrogen electrode, the specific activity for CO reduction to ethanol and acetate was linearly proportional to the fraction of NP surfaces comprised of GB surface terminations. Our results provide a design principle for CO reduction to ethanol and acetate on Cu. GB-rich Cu/CNT electrodes are the first NP catalysts with significant CO reduction activity at moderate overpotential, reaching a mass activity of up to ~1.5 A per gram of Cu and a Faradaic efficiency >70% at −0.3 V.
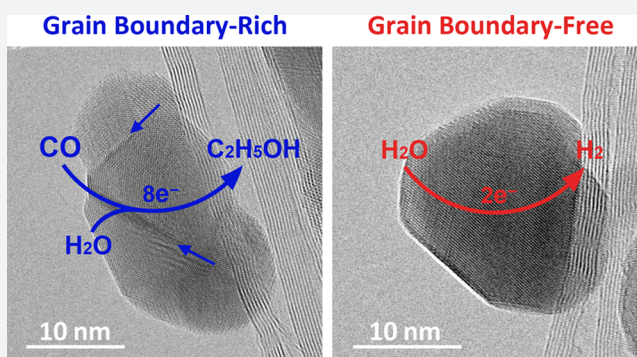
INTRODUCTION

Using renewable energy to power the reduction of CO_2 into fuels and chemicals is a possible value-added alternative to sequestration for mitigating CO_2 emissions.[1−4] Substantial progress has been made for the electrochemical conversion of CO_2 to CO; high temperature solid oxide cells catalyze this reaction at high current densities near the thermodynamic potential,[5] and new catalysts have enabled CO production in ambient-temperature cells at modest overpotentials.[6−14] Leveraging these advances requires efficient catalysts that further reduce CO to make energy-dense, high value chemicals and fuels. Cu is the only material known to have appreciable activity for electrochemical CO reduction to high-value products including ethanol, acetate, and propanol.[15,16] Unfortunately, conventional Cu electrodes such as foils and commercial nanoparticles (NPs) have low specific activity (activity per Cu surface area) and low selectivity for CO reduction vs H_2O reduction unless large overpotentials are applied. Large overpotentials result in low energy conversion efficiency and favor hydrocarbon products over liquid oxygenates. Making CO reduction practical requires drastically improving the catalytic properties of Cu and translating these improvements to NPs to minimize catalyst loading.

The equilibrium potentials for CO reduction to hydrocarbons and oxygenates are all >0 V vs reversible hydrogen electrode (RHE) (all potentials here are reported with respect

to this reference). Early electrolysis studies showed that polycrystalline Cu electrodes reduce CO to a mixture of hydrocarbons and oxygenates with a combined Faradaic efficiency of ~50% at < −0.9 V vs RHE (>1 V overpotential) in aqueous electrolytes.[15,16] Recent studies have examined polycrystalline and single-crystal Cu electrodes for CO reduction in sweep voltammetry at a wide range of potentials.[17−19] These studies have shown that Cu(111) electrodes do not reduce CO at potentials ≥ −1 V. By contrast, single-crystal Cu(100) electrodes show transient activity for CO reduction to ethylene from −0.3 V to −0.5 V.[17] However, sustained activity in bulk electrolysis has not been demonstrated for Cu(100) electrodes in this potential range.

We recently showed that Cu films prepared from Cu oxide precursors ("oxide-derived Cu") have enhanced specific CO reduction activity and suppressed specific H_2O reduction activity at moderate overpotential compared to other known Cu electrodes. At only −0.3 V, oxide-derived Cu reduces CO to ethanol and acetate with up to 57% Faradaic efficiency in sustained bulk electrolysis.[20−22] Oxide-derived Cu is a continuous metal film composed of 10−100 nm crystallites linked by grain boundaries (GBs), which suggests that the GBs

(a) Cu/CNT_as-dep   **(b)** Cu/CNT_200   **(c)** Cu/CNT_300   **(d)** Cu/CNT_400   **(e)** Cu/CNT_500
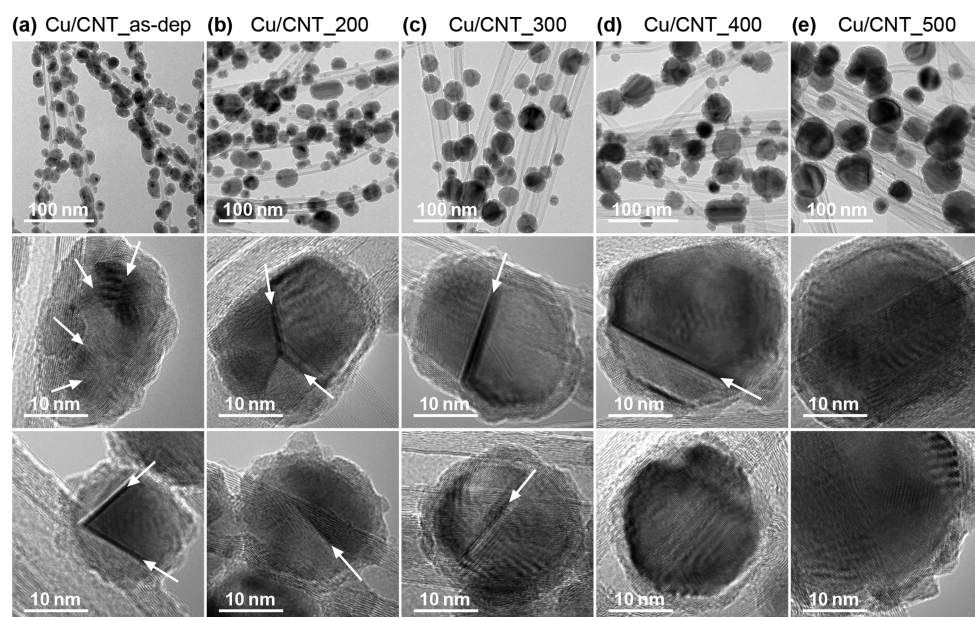

Figure 1. TEM characterization of Cu nanoparticles in the Cu/CNT electrodes. The five columns are the as-deposited Cu/CNT electrode (a) and the electrodes annealed under N_2 at 200 °C (b), 300 °C (c), 400 °C (d), and 500 °C (e). Top row: overview TEM images; middle and bottom rows: representative high-resolution TEM images. The arrows indicate the gain boundaries.

Table 1. Structural Metrics of As-Deposited and Annealed Cu/CNT Electrodes[a]

sample	particle size (nm)	GB surface density (μm^{-1})	microstrain (%)	grain size (nm)	surface area ($cm^2\ mg^{-1}$)
Cu/CNT_as-dep	16.9 ± 4.0	40.6 ± 4.3	0.17 ± 0.02	10.6	218 ± 4
Cu/CNT_200	19.5 ± 4.5	21.7 ± 2.1	0.10 ± 0.02	12.5	221 ± 6
Cu/CNT_300	22.1 ± 5.3	13.5 ± 1.2	0.07 ± 0.01	13.9	212 ± 5
Cu/CNT_400	26.3 ± 6.9	6.7 ± 0.6	0.05 ± 0.01	15.6	187 ± 5
Cu/CNT_500	33.6 ± 8.4	3.1 ± 0.2	0.02 ± 0.01	19.8	148 ± 6

[a]Particle size and GB surface density were quantified by TEM. Microstrain and grain size were determined by performing Williamson−Hall analysis of the X-ray diffraction patterns. Surface area was determined by measuring the electrochemical capacitance.

may be responsible for its unusual catalytic properties.[23] Quantifying the role of GBs in Cu-catalyzed CO reduction is essential for establishing a firm design principle, but it is difficult to quantify and modulate GBs in oxide-derived metals. It is also unclear if the factors that promote activity for a metallic film will be applicable to NPs, which are essential for electrolytic applications because of their high surface-area-to-mass ratios. We recently used vapor deposition and thermal annealing to prepare Au NPs on CNTs with different GB densities and showed that the activity for CO_2 reduction to CO was correlated with the coverage of GB surface terminations.[24] Using a similar strategy, here we show that GBs engender high activity for CO reduction on Cu, a more difficult and potentially more enabling transformation.

■ RESULTS AND DISCUSSION

Cu/CNT samples were prepared by depositing Cu at a nominal thickness of 10 nm onto a film of superaligned CNTs[25,26] using e-beam evaporation (Figure S1). X-ray photoelectron spectroscopy of the material showed the expected signals for C, Cu, and O (Figure S2). The Cu peaks indicated a mixture of Cu^0 and Cu^{1+}, the latter the result of Cu_2O formation from air exposure. Transmission electron microscopy (TEM) showed that the CNTs were decorated with Cu NPs (Figure 1a, top). Most of the NPs were composed of multiple Cu crystallites connected by GBs (Figure 1a, middle and bottom). The average particle size was 16.9 ± 4.0 nm (Table 1 and Figure S3). To quantify

the GBs, high-resolution TEM images were obtained for 200 NPs (Figure S4). For each NP image, the length of GBs and the particle area were measured. The GB quantity of interest is the fraction of the NP surfaces that corresponds to GB surface terminations (hereafter this fraction is referred to as the "GB surface density"). Because the TEM images are two-dimensional (2D) projections of three-dimensional (3D) particles, the measured GB lengths and particle areas were converted to GB surface termination lengths and 3D particle surface areas using conversion factors derived from simple geometrical models (see Supporting Information). The GB surface density was taken to be the sum of the GB surface lengths over all of the imaged NPs divided by the sum of the 3D particle surface areas. The value obtained for an as-deposited Cu/CNT sample (Cu/CNT_as-dep) was 40.6 ± 4.3 μm^{-1}. Measuring the GB surface density in this way is sufficient to determine the relative density between samples prepared in different ways to assess its relationship to catalytic activity (see below). Assuming a GB width of 1 nm, the measured GB surface density corresponds to a ~4% coverage of GB surface terminations.

To change the microstructure of the Cu NPs, Cu/CNT samples were annealed under N_2 at 200 °C, 300 °C, 400 °C, or 500 °C (Cu/CNT_200, Cu/CNT_300, Cu/CNT_400, and Cu/CNT_500). As seen by TEM, the number of GBs in the Cu NPs decreased as the annealing temperature was increased (Figure 1). To quantify the GB surface densities of the annealed samples, high-resolution TEM images of 200 NPs
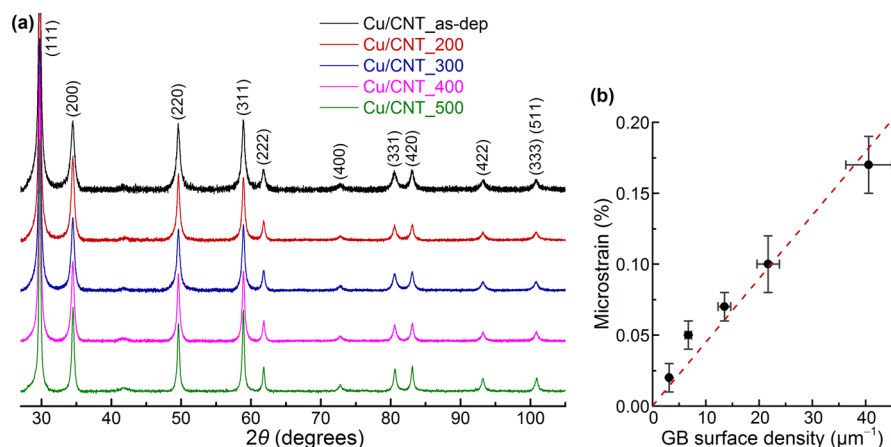
Figure 2. Grazing-incidence X-ray diffraction of Cu/CNT electrodes. (a) X-ray diffraction patterns for the as-deposited and annealed Cu/CNT electrodes. The very small peaks at $2\theta = 41.7°$ are attributed to native oxide formed during sample preparations. (b) Correlation between the microstrain extracted from Williamson−Hall analysis and the GB surface density.
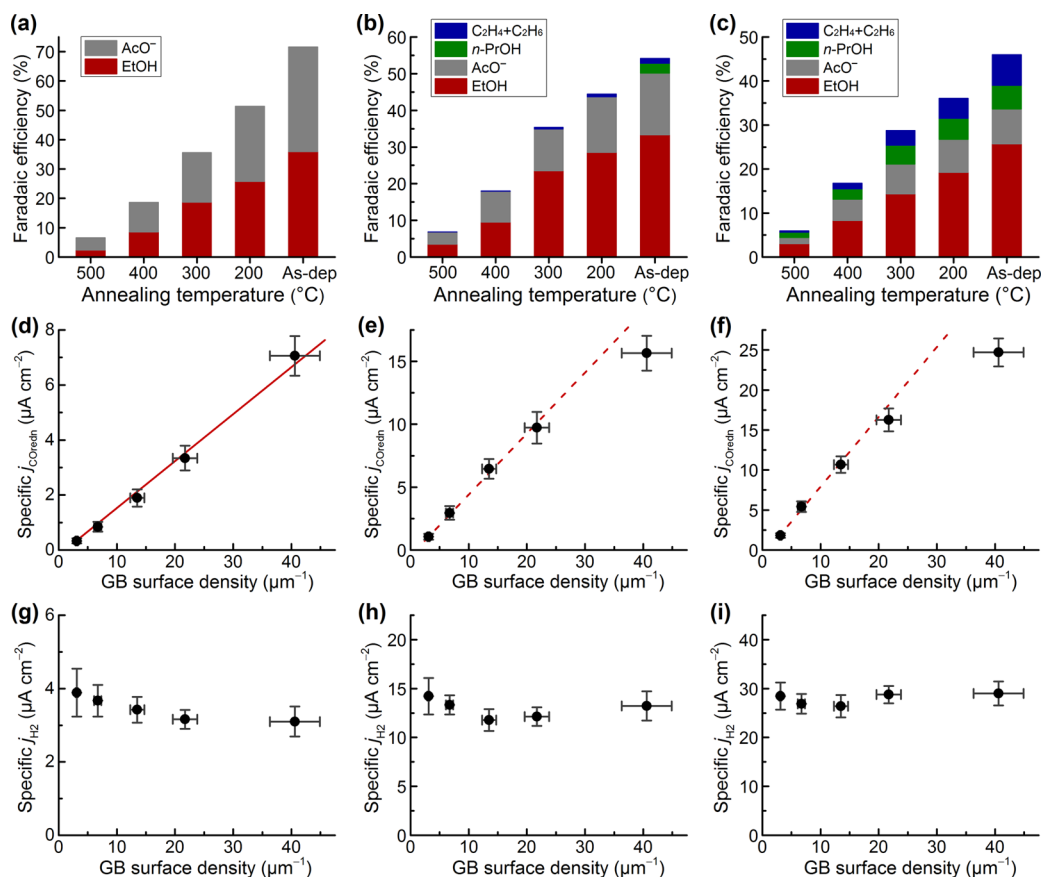

Figure 3. Correlation between the GB surface density and CO reduction activity. (a−c) Faradaic efficiencies for CO reduction products on the five Cu/CNT electrodes. The remaining Faradaic efficiency corresponds to H$_2$ evolution. (d−f) Specific activity for CO reduction vs the GB surface density. (g−i) Specific activity for H$_2$ evolution vs the GB surface density. The potentials are −0.3 V (a, d, g), −0.4 V (b, e, h), and −0.5 V (c, f, i) vs RHE.

from each sample were analyzed as described above (Figures S5−S8). The GB surface density decreased monotonically with temperature from 40.6 ± 4.3 μm^{-1} for Cu/CNT_as-dep to 3.1 ± 0.2 μm^{-1} for Cu/CNT_500 (Table 1). Annealing also caused a small amount of particle growth, with a maximum size of 33.6 ± 8.4 nm obtained for Cu/CNT_500 (Table 1). A previous analysis of size effects showed that reducing the diameter of Cu NPs below 5 nm changes the surface faceting

and distribution of coordination numbers at the surface, but there are no effects for sizes >5 nm. Moreover, size was reported to affect electrocatalytic activity only for NPs < 5 nm, which showed a ~2-fold increase in activity but no change in selectivity.[27] The particles of all of the Cu/CNT samples studied here are much larger than this size regime.[27]

To further characterize the effects of annealing Cu/CNT, TEM videos of individual NPs in the samples were obtained at

500 °C (Figure S9; videos S1 and S2). The videos show that GBs are lost via migration. Apart from GB loss, the overall structure of the NPs remains relatively unaffected.

To complement the microstructural analysis by TEM, powder X-ray diffraction patterns were obtained for all Cu/CNT samples in grazing incidence mode using synchrotron radiation at 11.5 keV. All of the patterns showed 11 peaks at the expected diffraction angles for metallic Cu and a very small Cu oxide peak attributed to native oxide formation during the sample preparations (Figure 2a). Line shape analysis of the diffraction patterns was performed using the Williamson–Hall method to determine the average crystallite size and microstrain (Figure S10). The average crystallite sizes increased with annealing temperature from 10.6 nm for Cu/CNT_as-dep to 19.8 nm for Cu/CNT_500 (Table 1). These sizes are smaller than the particle sizes measured by TEM because the particles are composed of multiple crystallites. The amount of microstrain was relatively high at 0.17% for Cu/CNT_as-dep and decreased with annealing temperature down to a small residual value of 0.02% for Cu/CNT_500 (Table 1). The microstrain was correlated with the GB surface density (Figure 2b). This correlation may reflect the strain imposed by GBs on the adjacent lattice regions[28] or the presence of dislocations associated with the GBs.[29] As such, the microstrain values extracted from X-ray diffraction line shape analysis provide an indirect measurement of relative GB density in the Cu/CNT samples that corroborates the quantification by TEM.

Cu/CNT films were rolled into yarns and connected to Cu wires for electrochemical measurements. The electrochemical Cu surface areas were estimated by measuring the double layer capacitance in 0.1 M HClO$_4$ (Figure S11).[30] Compared to Cu/CNT_as-dep, annealing the Cu/CNT films up to 300 °C had minimal effect on the surface area and annealing at 400 and 500 °C reduced the surface area by only 14 and 32%, respectively (Table 1). Because the Cu surface areas and particle sizes are comparable, the Cu/CNT samples enable GB effects to be studied independently of major morphological changes.

The CO reduction activity of Cu/CNT electrodes was assessed using constant-potential electrolysis lasting several hours in CO-saturated 0.1 M KOH electrolyte (Figure S12). The use of alkaline electrolyte is favorable because water is the only available H$^+$ donor for HER, and, at a fixed potential vs RHE, the driving force for electron transfer is increased as the pH is increased. The gas-phase products were quantified by periodic gas chromatography of the headspace, and the solution phase products were quantified at the end of each experiment by nuclear magnetic resonance (NMR) spectroscopy of the electrolyte (Figure S13). Figure 3a–c shows the Faradaic efficiencies for the CO reduction products on the five Cu/CNT electrodes at three different potentials. The remaining Faradaic efficiency up to 100% corresponds to H$_2$ evolution. At all potentials, the selectivity for CO vs H$_2$O reduction was the highest for Cu/CNT_as-dep and decreased monotonically as the annealing pretreatment temperature was increased. Cu/CNT_as-dep reached a peak value of 72% combined Faradaic efficiency for ethanol and acetate (28% H$_2$) at −0.3 V, the highest value reported to date for CO reduction. Ethylene, ethane, and propanol were additional CO reduction products at more negative potentials. In contrast, Cu/CNT_500 had less than 7% Faradaic efficiency for CO reduction (93% H$_2$) at all potentials, which was similar to commercial Cu NPs evaluated previously.[20] The background current for a CNT film without

Cu NPs was <5% of the value for the Cu/CNT electrodes, and the only product observed was H$_2$.

The different Faradaic efficiencies for the Cu/CNT electrodes resulted from different CO reduction activities, which were strongly dependent on the GB surface densities. Figure 3d–f shows the surface area–normalized CO reduction current densities (specific j_{COredn}) vs the GB surface densities for the Cu/CNT electrodes at −0.3 V, −0.4 V, and −0.5 V. At −0.3 V, j_{COredn} was linearly proportional to the GB surface density across all samples ($R^2 = 0.990$). At −0.4 V and −0.5 V, the relationship was linear for four of the samples and deviated from linearity for Cu/CNT_as-dep, the most GB-rich sample. This deviation is because the reduction kinetics depend, in part, on CO mass transport at the highest j_{COredn} values. All of the plots have intercepts very close to 0, suggesting that essentially all of the CO reduction activity from −0.3 V to −0.5 V arises from surface sites created by GBs.

In contrast to CO reduction, GB surface density had very little effect on H$_2$O reduction in either CO-saturated electrolyte (Figure 3g–i) or N$_2$-saturated electrolyte (Figure S14). These results indicate that H$_2$O reduction occurs primarily on low-index Cu facets. Although the GB surface density changes by more than an order of magnitude across the series, GB surface terminations are a minor fraction of the surface in all cases. The majority of the surfaces are likely comprised of low-index facets.

The CO reduction activity of the GB-rich Cu/CNT_as-dep electrode compares favorably with oxide-derived Cu, which was previously the most active known catalyst for this reaction. j_{COredn} was 3–6-fold higher on Cu/CNT_as-dep than oxide-derived Cu electrodes when evaluated under the same conditions at −0.3 V to −0.5 V (Figure 4a).[20] The FE was also higher for Cu/CNT_as-dep (Figure 4b), although this difference was much smaller than the difference in j_{COredn} because oxide-derived Cu electrodes suppress H$_2$O reduction
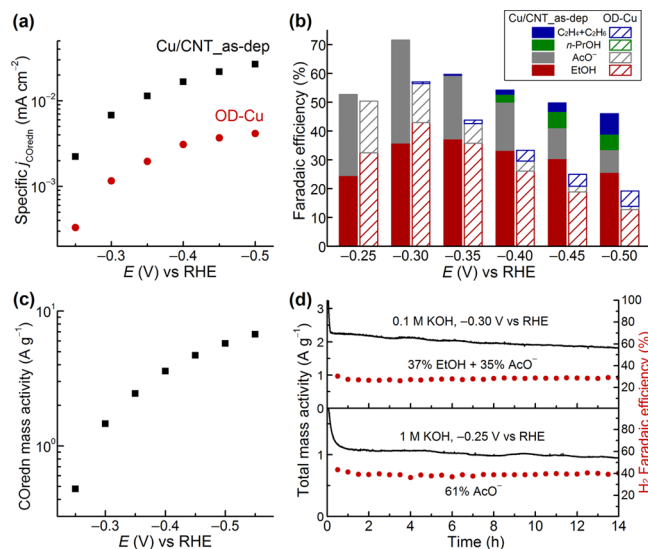

Figure 4. Performance of Cu/CNT_as-dep, the electrode with the highest GB surface density. (a, b) Comparison of the specific activity for CO reduction and Faradaic efficiencies for CO reduction products between Cu/CNT_as-dep and oxide-derived Cu. (c) Mass activity for CO reduction at selected potentials for Cu/CNT_as-dep. (d) Total mass activity over time (black, left-axis) and Faradaic efficiency for H$_2$ evolution over time (red, right-axis) for Cu/CNT_as-dep at −0.30 V vs RHE in 0.1 M KOH electrolyte and at −0.25 V in 1 M KOH electrolyte, as indicated.

but Cu/CNT_as-dep does not. The mass loading for Cu/CNT electrodes is extremely low compared to oxide-derived Cu, enabling much more efficient utilization of Cu. The steady-state mass activity (CO reduction current per Cu mass) of Cu/CNT_as-dep was 1–7 A g^{-1} from −0.3 to −0.55 V (Figure 4c). These values set benchmarks for future development of NP CO reduction catalysts. The geometric current density for CO reduction (geometric j_{COredn}) with Cu/CNT depends on the catalyst loading and the electrode geometry (Figure S15). With 0.6 mg Cu/CNT stretched over 2 cm^2 (∼120 cm^2 of Cu surface area), the geometric j_{COredn} was 0.37 mA/cm^2 at −0.3 V, a value approaching the mass transport limit in the cell. Higher mass activities and j_{COredn} may be possible with better delivery of CO to the NP surfaces.

The FE for CO reduction on Cu/CNT_as-dep is unchanged, and the mass activity exhibits only a slight decline over electrolysis lasting several hours (Figure 4d), indicating that the GBs are relatively stable under electrocatalytic conditions (Figure S16). Notably, the selectivity for ethanol vs acetate depends on the pH. As seen previously for oxide-derived Cu, acetate is the exclusive CO reduction product for Cu/CNT_as-dep at low overpotential when the electrolyte is switched from 0.1 to 1 M KOH (Figures 4d and S17).

The strong correlation between GB surface density and CO electroreduction activity suggests that GBs alter the surface properties of the particle to lower the barrier for this reaction. We recently found using temperature-programmed desorption that the surfaces of oxide-derived Cu contain binding sites for CO that are stronger (by ∼7 kJ mol^{-1}) than the sites on terraces or stepped surfaces.[23] We postulate that the GBs in Cu/CNT also create surfaces with strong CO binding sites and that these surfaces are responsible for the catalytic activity. Recent theoretical studies of CO reduction on Cu have proposed a rate-limiting reductive CO dimerization step,[18,31] which would be accelerated by increasing the CO binding strength. Further elucidation of the mechanism by which GBs affect catalysis will require atomic level structural elucidation of GB surface terminations.[32] Ideally, the surface structures will be probed under operating conditions to account for restructuring induced by the application of a voltage.[33] Researchers have previously proposed that stacking faults—a different kind of bulk defect—support active sites for CO hydrogenation to methanol on Cu NPs based on a correlation between activity and stacking fault probability determined by diffraction pattern analysis.[34−36]

CONCLUSION

Using bulk electrolysis and TEM measurements, we have shown that the steady-state, specific CO reduction activity on Cu NPs at moderate overpotential is correlated to the density of GBs. The quantitative correlation and near-zero activity in the limit of no GBs suggests that GBs are responsible for creating the vast majority of the active surfaces in this potential regime. Previously, GB engineering has been utilized with great success to change the mechanical properties of bulk metals.[37−40] Because nearly all of the GBs in a bulk material are buried, very little attention has been given to their effects on surface properties. The results here show the potential of using GBs to create persistent, catalytically active surfaces on NPs in the context of an especially demanding reaction. Exploiting GB effects for fuel synthesis and other chemistry will be aided by surface structure elucidation and new synthetic methods for preparing highly polycrystalline NPs.

ASSOCIATED CONTENT

Ⓢ Supporting Information

The Supporting Information is available free of charge on the ACS Publications website at DOI: 10.1021/acscentsci.6b00022.

> Materials, experimental methods, supporting data (Figures S1−S18) (PDF)
> Videos S1 (AVI) and S2 (AVI)

AUTHOR INFORMATION

Corresponding Author
*E-mail: mkanan@stanford.edu.

Notes

The authors declare no competing financial interest.

ACKNOWLEDGMENTS

REFERENCES

(1) Peters, M.; Köhler, B.; Kuckshinrichs, W.; Leitner, W.; Markewitz, P.; Müller, T. E. Chemical technologies for exploiting and recycling carbon dioxide into the value chain. *ChemSusChem* **2011**, *4*, 1216−1240.

(2) Graves, C.; Ebbesen, S. D.; Mogensen, M.; Lackner, K. S. Sustainable hydrocarbon fuels by recycling CO$_2$ and H$_2$O with renewable or nuclear energy. *Renewable Sustainable Energy Rev.* **2011**, *15*, 1−23.

(3) Aresta, M.; Dibenedetto, A.; Angelini, A. Catalysis for the valorization of exhaust carbon: from CO$_2$ to chemicals, materials, and fuels. Technological use of CO$_2$. *Chem. Rev.* **2014**, *114*, 1709−1742.

(4) Singh, M. R.; Clark, E. L.; Bell, A. T. Thermodynamic and achievable efficiencies for solar-driven electrochemical reduction of carbon dioxide to transportation fuels. *Proc. Natl. Acad. Sci. U. S. A.* **2015**, *112*, E6111−E6118.

(5) Bidrawn, F.; Kim, G.; Corre, G.; Irvine, J. T. S.; Vohs, J. M.; Gorte, R. J. Efficient reduction of CO$_2$ in a solid oxide electrolyzer. *Electrochem. Solid-State Lett.* **2008**, *11*, B167−B170.

(6) Costentin, C.; Robert, M.; Saveant, J. M. Catalysis of the electrochemical reduction of carbon dioxide. *Chem. Soc. Rev.* **2013**, *42*, 2423−2436.

(7) Qiao, J.; Liu, Y.; Hong, F.; Zhang, J. A review of catalysts for the electroreduction of carbon dioxide to produce low-carbon fuels. *Chem. Soc. Rev.* **2014**, *43*, 631−675.

(8) Lu, Q.; Rosen, J.; Jiao, F. Nanostructured metallic electrocatalysts for carbon dioxide reduction. *ChemCatChem* **2015**, *7*, 38−47.

(9) Schreier, M.; Curvat, L.; Giordano, F.; Steier, L.; Abate, A.; Zakeeruddin, S. M.; Luo, J.; Mayer, M. T.; Grätzel, M. Efficient photosynthesis of carbon monoxide from CO$_2$ using perovskite photovoltaics. *Nat. Commun.* **2015**, *6*, 7326.

(10) Chen, Y.; Li, C. W.; Kanan, M. W. Aqueous CO$_2$ reduction at very low overpotential on oxide-derived Au nanoparticles. *J. Am. Chem. Soc.* **2012**, *134*, 19969−19972.

(11) Tornow, C. E.; Thorson, M. R.; Ma, S.; Gewirth, A. A.; Kenis, P. J. Nitrogen-based catalysts for the electrochemical reduction of CO$_2$ to CO. *J. Am. Chem. Soc.* **2012**, *134*, 19520−19523.

(12) Medina-Ramos, J.; DiMeglio, J. L.; Rosenthal, J. Efficient reduction of CO$_2$ to CO with high current density using in situ or ex situ prepared Bi-based materials. *J. Am. Chem. Soc.* **2014**, *136*, 8361−8367.

(13) Lu, Q.; Rosen, J.; Zhou, Y.; Hutchings, G. S.; Kimmel, Y. C.; Chen, J.; Jiao, F. A selective and efficient electrocatalyst for carbon dioxide reduction. *Nat. Commun.* **2014**, *5*, 3242.

(14) Asadi, M.; Kumar, B.; Behranginia, A.; Rosen, B. A.; Baskin, A.; Repnin, N.; Pisasale, D.; Phillips, P.; Zhu, W.; Haasch, R.; et al. Robust

carbon dioxide reduction on molybdenum disulphide edges. *Nat. Commun.* **2014**, *5*, 4470.

(15) Hori, Y.; Murata, A.; Takahashi, R.; Suzuki, S. Electroreduction of CO to CH_4 and C_2H_4 at a copper electrode in aqueous-solutions at ambient-temperature and pressure. *J. Am. Chem. Soc.* **1987**, *109*, 5022−5023.

(16) Hori, Y.; Takahashi, R.; Yoshinami, Y.; Murata, A. Electrochemical reduction of CO at a copper electrode. *J. Phys. Chem. B* **1997**, *101*, 7075−7081.

(17) Schouten, K. J. P.; Qin, Z.; Gallent, E. P.; Koper, M. T. M. Two pathways for the formation of ethylene in CO reduction on single-crystal copper electrodes. *J. Am. Chem. Soc.* **2012**, *134*, 9864−9867.

(18) Calle-Vallejo, F.; Koper, M. T. M. Theoretical considerations on the electroreduction of CO to C_2 species on Cu(100) electrodes. *Angew. Chem., Int. Ed.* **2013**, *52*, 7282−7285.

(19) Schouten, K. J. P.; Gallent, E. P.; Koper, M. T. M. Structure sensitivity of the electrochemical reduction of carbon monoxide on copper single crystals. *ACS Catal.* **2013**, *3*, 1292−1295.

(20) Li, C. W.; Ciston, J.; Kanan, M. W. Electroreduction of carbon monoxide to liquid fuel on oxide-derived nanocrystalline copper. *Nature* **2014**, *508*, 504−507.

(21) Li, C. W.; Kanan, M. W. CO_2 reduction at low overpotential on Cu electrodes resulting from the reduction of thick Cu_2O films. *J. Am. Chem. Soc.* **2012**, *134*, 7231−7234.

(22) Bertheussen, E.; Verdaguer-Casadevall, A.; Ravasio, D.; Montoya, J. H.; Trimarco, D. B.; Roy, C.; Meier, S.; Wendland, J.; Nørskov, J. K.; Stephens, I. E. L.; et al. Acetaldehyde as an intermediate in the electroreduction of carbon monoxide to ethanol on oxide-derived copper. *Angew. Chem., Int. Ed.* **2016**, *55*, 1450−1454.

(23) Verdaguer-Casadevall, A.; Li, C. W.; Johansson, T. P.; Scott, S. B.; McKeown, J. T.; Kumar, M.; Stephens, I. E. L.; Kanan, M. W.; Chorkendorff, I. Probing the active surface sites for CO reduction on oxide-derived copper electrocatalysts. *J. Am. Chem. Soc.* **2015**, *137*, 9808−9811.

(24) Feng, X.; Jiang, K.; Fan, S.; Kanan, M. W. Grain-boundary-dependent CO_2 electroreduction activity. *J. Am. Chem. Soc.* **2015**, *137*, 4606−4609.

(25) Jiang, K.; Wang, J.; Li, Q.; Liu, L.; Liu, C.; Fan, S. Superaligned carbon nanotube arrays, films, and yarns: A road to applications. *Adv. Mater.* **2011**, *23*, 1154−1161.

(26) Liu, K.; Sun, Y.; Chen, L.; Feng, C.; Feng, X.; Jiang, K.; Zhao, Y.; Fan, S. Controlled growth of super-aligned carbon nanotube arrays for spinning continuous unidirectional sheets with tunable physical properties. *Nano Lett.* **2008**, *8*, 700−705.

(27) Reske, R.; Mistry, H.; Behafarid, F.; Roldan Cuenya, B.; Strasser, P. Particle size effects in the catalytic electroreduction of CO_2 on Cu nanoparticles. *J. Am. Chem. Soc.* **2014**, *136*, 6978−6986.

(28) Stukowski, A.; Markmann, J.; Weissmuller, J.; Albe, K. Atomistic origin of microstrain broadening in diffraction data of nanocrystalline solids. *Acta Mater.* **2009**, *57*, 1648−1654.

(29) Van Swygenhoven, H.; Farkas, D.; Caro, A. Grain-boundary structures in polycrystalline metals at the nanoscale. *Phys. Rev. B* **2000**, *62*, 831−838.

(30) Waszczuk, P.; Zelenay, P.; Sobkowski, J. Surface interaction of benzoic acid with a copper electrode. *Electrochim. Acta* **1995**, *40*, 1717−1721.

(31) Montoya, J. H.; Shi, C.; Chan, K.; Nørskov, J. K. Theoretical insights into a CO dimerization mechanism in CO_2 electroreduction. *J. Phys. Chem. Lett.* **2015**, *6*, 2032−2037.

(32) Radetic, T.; Lancon, F.; Dahmen, U. Chevron defect at the intersection of grain boundaries with free surfaces in Au. *Phys. Rev. Lett.* **2002**, *89*, 085502.

(33) Kim, Y. G.; Baricuatro, J. H.; Javier, A.; Gregoire, J. M.; Soriaga, M. P. The evolution of the polycrystalline copper surface, first to Cu(111) and then to Cu(100), at a fixed CO_2RR potential: A study by operando EC-STM. *Langmuir* **2014**, *30*, 15053−15056.

(34) Kasatkin, I.; Kurr, P.; Kniep, B.; Trunschke, A.; Schlogl, R. Role of lattice strain and defects in copper particles on the activity of Cu/

ZnO/Al_2O_3 catalysts for methanol synthesis. *Angew. Chem., Int. Ed.* **2007**, *46*, 7324−7327.

(35) Behrens, M.; Studt, F.; Kasatkin, I.; Kühl, S.; Hävecker, M.; Abild-Pedersen, F.; Zander, S.; Girgsdies, F.; Kurr, P.; Kniep, B. L.; et al. The active site of methanol synthesis over Cu/ZnO/Al_2O_3 industrial catalysts. *Science* **2012**, *336*, 893−897.

(36) Kandemir, T.; Kasatkin, I.; Girgsdies, F.; Zander, S.; Kühl, S.; Tovar, M.; Schlogl, R.; Behrens, M. Microstructural and defect analysis of metal nanoparticles in functional catalysts by diffraction and electron microscopy: The Cu/ZnO catalyst for methanol synthesis. *Top. Catal.* **2014**, *57*, 188−206.

(37) Watanabe, T.; Tsurekawa, S. The control of brittleness and development of desirable mechanical properties in polycrystalline systems by grain boundary engineering. *Acta Mater.* **1999**, *47*, 4171−4185.

(38) Meyers, M. A.; Mishra, A.; Benson, D. J. Mechanical properties of nanocrystalline materials. *Prog. Mater. Sci.* **2006**, *51*, 427−556.

(39) Lu, L.; Sui, M. L.; Lu, K. Superplastic extensibility of nanocrystalline copper at room temperature. *Science* **2000**, *287*, 1463−1466.

(40) Champion, Y.; Langlois, C.; Guérin-Mailly, S.; Langlois, P.; Bonnentien, J. L.; Hÿtch, M. J. Near-perfect elastoplasticity in pure nanocrystalline copper. *Science* **2003**, *300*, 310−311.